J Mater Sci

Metals & corrosion

Diffusion in the liquid Al–In alloy when approaching the miscibility gap

Toni Schiller[1], Benedikt Reiplinger[1], Asbjørn Torsvik Krüger[1], Elke Sondermann[1,*], and Andreas Meyer[1]

[1] *Institute for Frontier Materials on Earth and in Space, German Aerospace Center (DLR), Linder Höhe, 51147 Cologne, Germany*

Received: 2 December 2025
Accepted: 31 August 2026

ABSTRACT

Monotectic alloys offer the potential to produce materials with exceptional functional properties due to their demixing behavior. To understand and control the formation of the final microstructure, knowledge of the dynamics near the miscibility gap is required. We measured interdiffusion in liquid Al–In using a combination of X-ray radiography and a shear cell furnace, which allows in situ observation of the diffusion process. While the temperature dependence of interdiffusion can be described by an Arrhenius function, its concentration dependence is unexpectedly weak. From thermodynamics, a steep decrease of interdiffusion close to the miscibility gap is expected. However, the kinetic behavior of the liquid alloy, mainly determined by the self-diffusion coefficients, seems to largely compensate for this decrease. This finding is supported by additional density measurements. Studying the density in liquid Al–In up to a concentration of 20 at% In at temperatures between 850 and 1400 K shows that the temperature dependence of density, as well as the thermal expansion, for each alloy composition under consideration is the same inside and outside the miscibility gap. Significant deviation from ideality is obtained for the concentration dependences of density. This is reflected in a negative excess volume.

Introduction

Multicomponent alloys with a miscibility gap in the liquid state, also called monotectic alloys, are of interest in basic and applied research for the development of structured materials [1–4]. The microstructure generated due to phase separation [2, 5–7] can produce novel materials with exceptional functional properties or e.g., increased yield strength [8]. Such materials can be produced using techniques such as casting or additive manufacturing [9, 10].

In order to be able to generate the microstructure and the volume ratios of the coexisting phases in a controlled manner, not only the choice of composition is crucial, but also the quenching dynamics [1, 11]. Several alloys, e.g., Al–In, Bi–Ga, Cu–Pb, show

Handling Editor: Megumi Kawasaki.

Address correspondence to E-mail: elke.sondermann@dlr.de

E-mail Addresses: toni_schiller@gmx.net; benedikt.reiplinger@dlr.de; asbjorn.kruger@gmail.com; andreas.meyer@dlr.de

https://doi.org/10.1007/s10853-026-13727-3
Published online: 21 September 2026

a miscibility gap in the liquid state. Such alloy systems exhibit large positive enthalpy of mixing and a preference of like atoms as nearest neighbors [12, 13]. Phase separation in a strictly monotectic alloy system already occurs in the liquid state, resulting in a liquid–liquid phase separation.

For better control of the separation process, knowledge of these liquid–liquid demixing dynamics is crucial. However, there are hardly any experimental data on the dynamics of such liquid–liquid demixing metal systems [14–19].

Interdiffusion, also known as chemical diffusion, describes the transport of mass driven by a gradient in the chemical potential. In alloys that are fully miscible, this atomic transport leads to a reduction of concentration differences [20]. For the determination of interdiffusion coefficients in liquid alloys, the in situ shear cell method has been proven to yield accurate data. It allows an in situ X-ray investigation of binary alloy systems, providing space- and time-resolved information and excluding negative effects of melting and solidification [21–24]. Al–In was chosen for this study as it offers excellent X-ray contrast and also exhibits exemplary monotectic liquid–liquid demixing behavior [25].

The phase diagram of Al–In is shown in Fig. 1. The boundary line of the miscibility gap in the phase diagram denotes the compositions and temperatures at which the alloy changes from a mixed liquid state to a demixed liquid state. When approaching the miscibility gap, either by changing the composition of the alloy or by reducing the temperature of the melt in the relevant composition range, the tendency for mixing is reduced. This tendency is reflected in the thermodynamic factor which is derived from the Gibbs energy. For ideal systems the thermodynamic factor is unity, but when approaching the miscibility gap, it tends to zero. Interdiffusion can be represented by a kinetic contribution that contains the self-diffusion coefficients, multiplied by the thermodynamic factor. Consequently, the interdiffusion coefficient is expected to decrease when approaching the miscibility gap.

We present interdiffusion measurements for the Al–In system at different Al-rich compositions and at different temperatures near the miscibility gap. Interdiffusion measurements were conducted in the miscible phase except for two measurements that were done at the boundary line of the miscibility gap.

Denser liquids show slower diffusion behavior due to a decrease in the free volume [26, 27]. Therefore, complementary density data for Al-rich Al–In are obtained with the electromagnetic levitation technique. This technique bypasses the drawbacks of conventional container-based measurement techniques such as reactions with container walls and contamination.

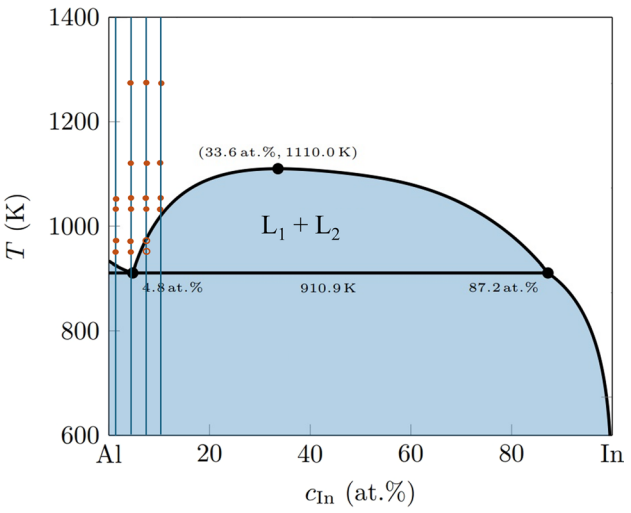

Figure 1 Phase diagram of Al–In. Temperatures and indium concentrations at which interdiffusion was measured are marked in orange.

Theoretical background

The interdiffusion coefficient D_{AB} in a binary alloy can be estimated from the two self-diffusion coefficients D_A, D_B, the concentrations c_A and c_B, and the thermodynamic factor, Φ, using the Darken equation [28]

$$D_{\mathrm{AB}} = \Phi S(c_B D_A + c_A D_B) \tag{1}$$

In the original Darken equation $S = 1$. Microscopic considerations showed that additional contributions to interdiffusion need to be included and that these contributions can be integrated in one factor S [29]. While in some liquid alloys, e.g., Al-rich Al–Cu [23], the factor S is close to unity, it contributes significantly in other alloys. For example in liquid Ni–Zr $S = 0.4$ was found for certain compositions [30]. When the Darken equation is applied to interdiffusion in crystals, a comparable factor, the Manning factor, is applied [31].

The different contributions to interdiffusion can be separated into a kinetic part $L = S(c_B D_A + c_A D_B)$

and a thermodynamic part Φ. In the microscopic description, the kinetic part is given by velocity autocorrelation functions.

The thermodynamic factor accounts for deviations from an ideal behavior due to chemical interactions and is equal to one for ideal mixtures. It is defined as the second derivative of the Gibbs energy G with respect to the concentration c where either c_A or c_B can be used:

$$\Phi = \frac{c(1-c)}{RT}\frac{\partial^2 G}{\partial c^2} \tag{2}$$

R and T are the molar gas constant and the absolute temperature, respectively. When approaching the miscibility gap, the thermodynamic factor tends to zero.

Experimental method

In situ shear cell technology

The in situ shear cell method makes use of the shear cell principle (e.g., [32, 33]) which ensures a defined start of the diffusion process and combines it with X-ray imaging for in situ information acquisition of the interdiffusion process [24].

After reaching the target temperature where the samples are fully liquid, a concentration gradient is generated via the shearing process by shifting the lower shear cell segment (see Fig. 2a). Once adjacent capillaries of different concentrations are brought together, a so-called diffusion couple is thus formed. It is initially characterized by a step function in the concentration distribution. The shearing process and the changes in the concentration profile are continuously monitored radiographically. This allows a smooth process control of the experiment, but also an in situ information acquisition of the interdiffusion process. For X-ray imaging, we use a microfocus X-ray source (XT9160-TED, Viscom AG, Hannover, Germany) operated at 150 kV and 250 μA and a CdTe detector with a 100 μm pixel size (XC-Thor series, Direct Conversion AB, Danderyd, Sweden). The effective pixel size for the experiment is ~ 50 μm and the effective frame rate 1 Hz. An X-ray image of the shear cell furnace after the shearing process is shown in Fig. 2b

The in situ shear cell method has been continuously improved over the past years [22, 34, 35]. In the current design (see Fig. 2a), there are four adjacent sample capillaries which then, through shifting, form three

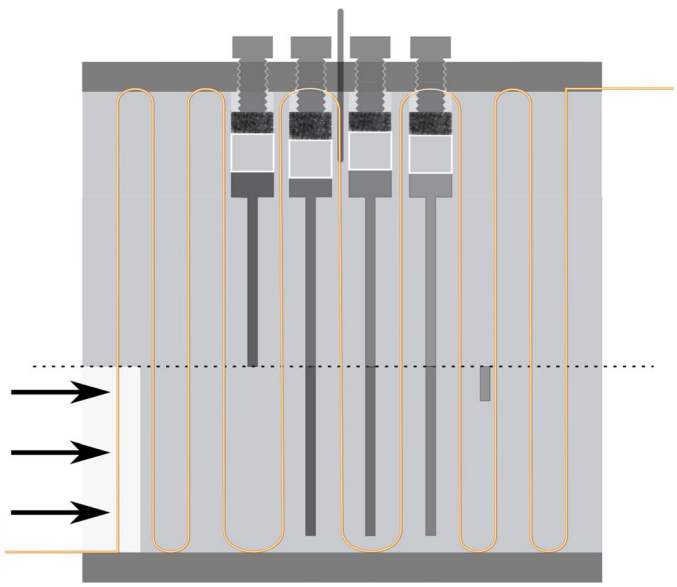

(a) Scheme

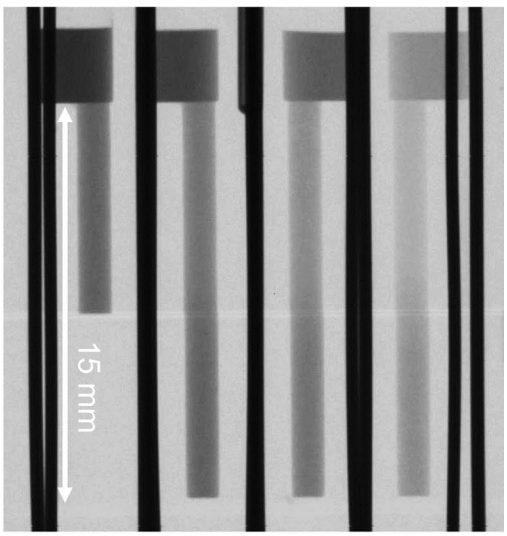

(b) X-ray image

Figure 2 **a** Scheme of an in situ shear cell furnace: The orange line shows the position of the heating wires. The dashed line represents the sliding plane. After reaching a stable state at target temperature, the lower part is shifted as indicated by the arrows to form three concentration couples and initiate the interdiffusion. **b** X-ray image of the shear cell furnace after shifting the lower part. The reservoirs at the top of the samples appear darker because they have a bigger diameter.

diffusion couples per experiment. For example, one shear cell contained the four samples with 0, 3, 6 and 9 at% In, resulting in three diffusion couples with the mean composition 1.5, 4.5 and 7.5 at% In.

Any perturbations of the concentration profile, due to e.g., shear convection at the beginning of an experiment, resolve within the first minute, so that ideally diffusion periods between 100 and 800 s after shifting can be used for the analysis. The capillary length is 26 mm and the capillary diameter is 1.3 mm. The shear cell itself is made of graphite, which ensures excellent heat conduction and an inert sample environment. During an experiment, a pressure of $< 5 \cdot 10^{-3}$ mbar is maintained, preventing oxidation processes and reducing heat dissipation. Essentially, the entire design is aimed at avoiding convection, which can distort the measured interdiffusion coefficients [36, 37].

Microgravity experiments have shown that with the in situ shear cell design, the systematic error due to possible density-driven convection is very small to non-existent under laboratory conditions for certain alloys [38]. Although other in situ methods exist for the determination of diffusion coefficients (e.g., in situ radiotracer [39] or in situ X-ray fluorescence [40]), the in situ shear cell method is the only method that offers spatial information over the full sample length and width in addition to the temporal resolution of the diffusion process, which makes it unique for this particular application.

Analysis of in situ shear cell method

The applied analyzing method was selected according to the X-ray contrast provided by the Al–In system for a concentration difference of 3 at%. This analyzing method can be applied also for sample systems with low contrast in the X-ray images. For other analyzing approaches see [22, 41, 42]. Prior to analysis, the detector photon counts will be converted to concentration profiles at each time step using references from Al–In alloys of known composition [24]. In this way, a data set of the concentration $c(x, t)$ as function of position x along the sample and time t is obtained as starting point for the analysis. Figure 3 shows such concentration profiles $c(x, t)$ for the diffusion pair 6 vs. 9 at% In at three different points in time.

For the given situation of a one-dimensional concentration distribution with an initial step function and infinite length, Fick's 2nd law of diffusion is solved by this equation [43]:

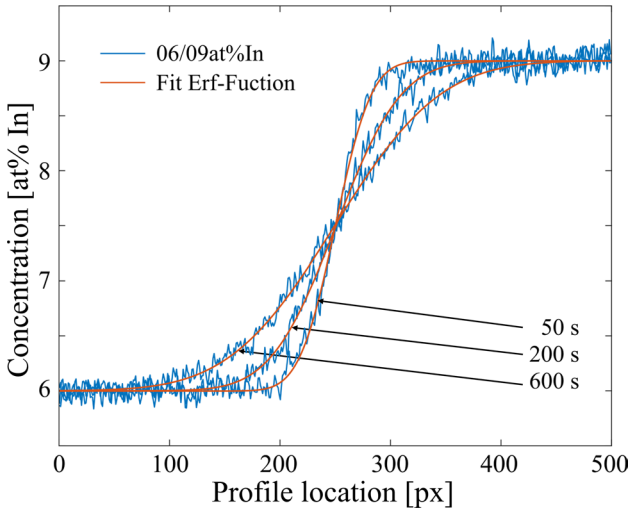

Figure 3 Concentration profiles of diffusion couple 6 versus 9 at%In at 1273 K for different diffusion times t. The Fit Erf-Function represents fitting through Eq. (3).

$$c(t,x) = \frac{c_1 + c_2}{2} + \frac{c_2 - c_1}{2} \operatorname{erf}\left(\frac{x - x_0}{\sqrt{4Dt}}\right) \tag{3}$$

The value x_0 marks the point-symmetric center of the distribution, while Dt is a measure for the width of the concentration profile and thus the progress of the diffusion process with time. No effects at the capillary ends are considered, which, however, would only occur if the diffusion had progressed very far in time (e.g., for $D = 10^{-8}$ m^2/s and a capillary length of $l_{cap} = 26$ mm the end of the capillary becomes relevant for times larger than ~ 1000 s). From the linear behavior of $Dt(t)$, the diffusion coefficient D can be determined (see Fig. 4).

The analysis yields an average diffusion coefficient D for the concentration range between the initial concentrations c_1 and c_2. According to Fick's 2nd law, the diffusion coefficient is assumed to be constant within the concentration range between c_1 and c_2. However, the diffusion coefficient usually shows a more or less pronounced concentration dependence [22, 23, 44]. If the diffusion coefficient is clearly concentration-dependent within the measurement range between c_1 and c_2, which means that the concentration gradient spreads faster in one direction than the other, this will lead to a systematic error in the analysis. A clear concentration dependence of the diffusion coefficient produces an asymmetry in the concentration distribution

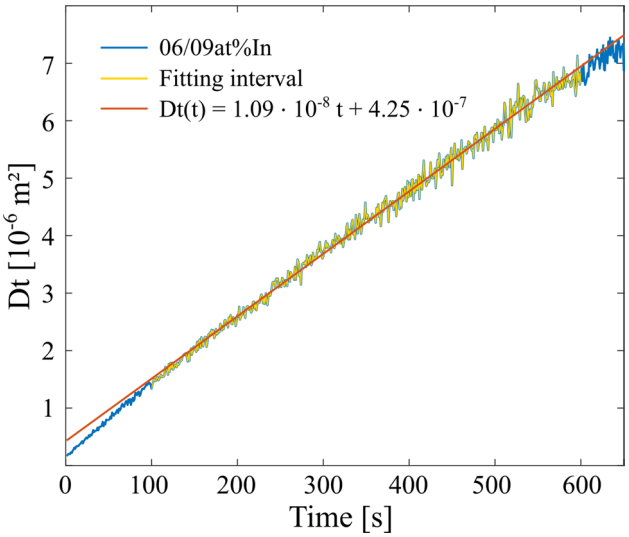

Figure 4 *Dt* values of experiment 6 versus 9 at%In at 1273 K from a series of fits as shown in Fig. 3 as a function of time. *Dt* values that are used for the linear fit are marked in yellow, and the red line shows the linear fit of the values.

over time. In this case, the left and right sides of the concentration distribution no longer behave point-symmetrically around the center x_0, resulting in a shift of the fit value x_0 over time. The stability of the x_0 value in Fig. 3 is thus an important quality parameter of the fitting routine, ensuring the correctness of the analytical approach used here.

The most important source of error in interdiffusion measurements is residual convection. In an earlier publication [45], we showed that analyzing the left, center and right part of the vertical capillary separately, gives a good estimate of the accuracy of the measurement. Measurements with relative errors of more than 15% were excluded from analysis.

Optical dilatometry method in electromagnetic levitation

For density measurements, the optical dilatometry method was used in combination with electromagnetic levitation (EML). The EML operation principle is based on an alternating, inhomogeneous magnetic field, which is generated by a water-cooled copper coil carrying a high-frequency alternating current with 200 A and approximately 250 kHz. The spherical metallic sample, usual diameters ranging from 5 to 7 mm, is placed inside the coil before the experiment is started. With the start of the experiment, eddy currents are induced inside the sample by the AC magnetic field. The sample is simultaneously heated and eventually molten, due to ohmic losses by the eddy currents, and levitated, due to the Lorentz force acting upon the induced currents. A laminar cooling gas flow with a high-purity inert gas mixture of Ar and He is used to adjust the temperature of the molten sample during the experiment. The density of the levitating molten droplet is determined by measuring its volume. To do this, an expanded laser beam projects a shadow graph image of the sample onto a CCD camera opposite to the laser source. The projections are analyzed in real time with an edge detection algorithm. Assuming an average spherical sample, the volume in pixels^3 is calculated, which is subsequently converted to the real volume based upon a previous calibration. Optical dilatometry in combination with EML is a well-established technique for the density determination of highly reactive metal melts. The container-less nature of the experiment circumvents the contamination risks associated with conventional container-based methods and offers the advantage of high possible undercoolings due to the absence of heterogeneous nucleation sites. A more in-depth description of the EML furnace and the exact optical setup used can be found in references [46–49].

A detailed uncertainty estimation for the density measurements using EML and the optical dilatometry method used in this work can be found in [50]. The main error sources are: mass loss (m), calibration (q) or temperature (T) error, strong sample movement and a distorted sample shape and symmetry (V_P). The usual total uncertainty is to be calculated using the formula

$$\frac{\Delta\rho^2}{\rho^2} = \frac{\Delta m^2}{m^2} + \frac{\Delta q^2}{q} + \frac{\Delta V_p^2}{V_p^2} + \left(\frac{\partial V_p}{\partial T}\right)^2 \frac{\Delta T^2}{V_p^2} \tag{4}$$

Experimental results and discussion

Concentration dependence of the interdiffusion coefficient

The interdiffusion of the Al–In system shows only a slight concentration dependence within the measured concentration range (see Fig. 5). Compared to the self-diffusion of pure aluminum $D_{\mathrm{Al}}(980K) = (7.2 \pm 0.6) \cdot 10^{-9}$ m^2/s determined via quasi-elastic neutron scattering [51], interdiffusion even at very low content of In occurs more slowly

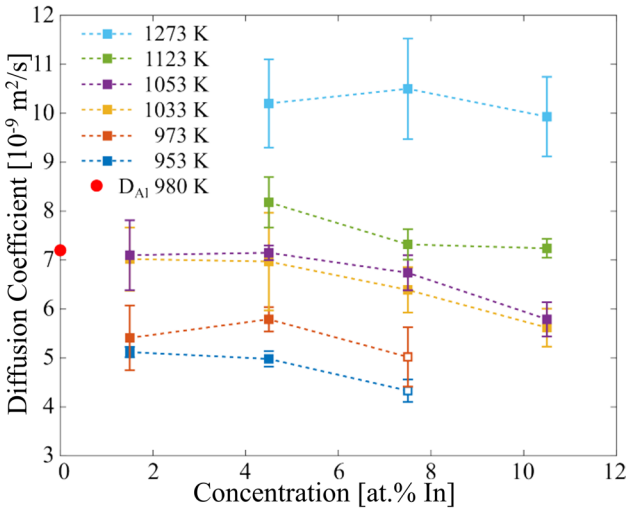

Figure 5 Interdiffusion coefficients of Al-rich Al–In as a function of the In concentration. Open squares refer to data measured in close proximity to the miscibility gap. The self-diffusion of pure Al [51] is shown for comparison.

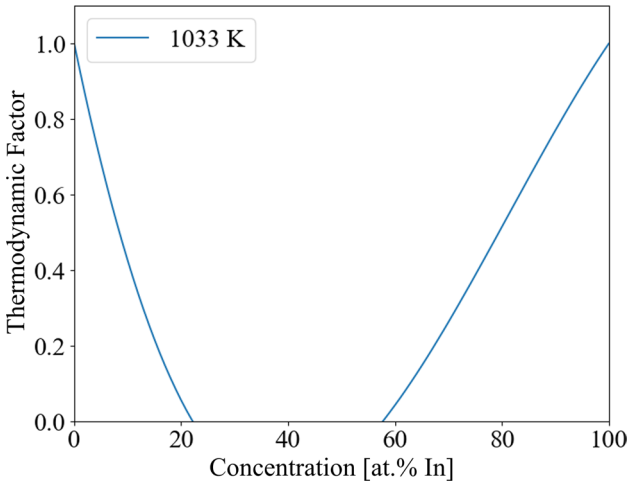

Figure 6 Thermodynamic factor Φ of Al–In at 1033 K according to Kaban et al. [54].

(by ~ 20%) at comparable temperatures. Such a drop in the dynamics even for very low concentrations has already been reported for other elements in liquid Al (e.g., Ni, Cu, Ag and Au [22, 23, 44, 52]).

Diffusion coefficients for pure indium have been reported by Foster et al. determined via capillary reservoir technique suggesting an In self-diffusion of $D_{\mathrm{In}}(1300K) = (9.1 \pm 1.1) \cdot 10^{-9}\ \mathrm{m}^2/\mathrm{s}$ [53]. It can be stated that the self-diffusion of pure indium seems to be slower than that of pure Al at the same T. Indium self-diffusion in pure indium is of similar magnitude (potentially slightly slower) as Al–In interdiffusion in the Al-rich regime.

On the In-rich side of the Al–In alloy, experiments using an ex situ shear cell furnace resulted in interdiffusion coefficients of $D(893K) = (8.4 \pm 1.5) \cdot 10^{-9}\ \mathrm{m}^2/\mathrm{s}$ and $D(953K) = (9.3 \pm 2.5) \cdot 10^{-9}\ \mathrm{m}^2/\mathrm{s}$, for 97.5at% In [16].

With increasing In content, the interdiffusion coefficient decreases only slightly. Calculations of the thermodynamic factor of the Al–In system based on the thermodynamic description by Kaban et al. [54] also suggest a different behavior (see Fig. 6). The thermodynamic factor decreases rapidly toward the miscibility gap. According to Darken's equation (see Eq. 1), interdiffusion in a binary mixture can be calculated from the two self-diffusion coefficients and the thermodynamic factor. Therefore, the concentration dependence of the thermodynamic factor should also be reflected in the interdiffusion coefficient, which it is not, based on our measurement results. For example, between 1.5 and 10.5 at% In at 1033 K the interdiffusion coefficient decreases by 20%, while the thermodynamic factor of Kaban et al. decreases by 50% in the same concentration range. This could be due to an increase of the factor S mentioned in Eq. (1) or due to an increase of the self-diffusion. A high self-diffusion coefficient of indium at the discussed Al-rich concentrations could counteract the influence of the thermodynamic factor on the interdiffusion and explain the weak concentration dependence. To the best of our knowledge, there are currently no data on self-diffusion in Al-rich Al–In melts. A low packing fraction is connected to high self-diffusion coefficients as atoms can move easier. Therefore, the density and the packing fraction of liquid Al–In will be discussed in "Density measurements" section.

Molecular dynamic simulations of demixing liquids are interesting to understand the general behavior. In molecular dynamic simulations of demixing Cu-Co melts, the self-diffusion of Cu is slightly larger than of Co and both values increase by more than a factor of 2 with increasing Cu-composition. Interdiffusion obtained from the Darken equation shows a minimum near the critical composition [55]. Molecular dynamic simulations of a binary Lennard–Jones mixture approaching a critical point showed that the self-diffusion did not show diverging behavior.

Shear viscosity and the interdiffusion on the other hand follow asymptotic power laws as predicted by mode-coupling theories [56].

After discussing the measurements of interdiffusion outside of the miscibility gap, we like to mention the two data points at the right-hand side of the measurements at 953 and 973 K, shown in Fig. 5 by open boxes. The concentration range of these experiments is right at the boundary line of the miscibility gap and was partially within the binodal liquid–liquid demixing regime. In the X-ray images, no separation could be resolved. It is possible that fine dispersed droplets of the minority phase formed in parts of the diffusion couple but did not agglomerate or sediment during the time of the experiment. The concentration profile along the diffusion couple was obtained the same was as for the other experiments. A mass transport along the capillary is apparent, which can be represented by a diffusion coefficient via the applied analysis. In this case, however, it is a mass transport superimposed by interdiffusion processes in the main phase and the self-diffusion of the dispersed droplets. Accordingly, these data points should not be seen as pure interdiffusion coefficients of the system.

Temperature dependence of the interdiffusion coefficient

Figure 7 shows the measured interdiffusion coefficients semilogarithmically as a function of inverse temperature. Due to the small concentration differences and the low concentration dependence of the interdiffusion, all data were fit with the same Arrhenius function:

$$D(T) = D_0 \exp(-E_A/k_B T) \tag{5}$$

Due to this averaging, the fitting results represent an average concentration of roughly 6at%In. From the Arrhenius fit, the average activation energy is E_A(6at% In) = 271 ± 27 meV. Comparing this to the activation energies of the pure elements E_A(Al) ≈ 280 meV [51] and E_A(In) ≈ 108 meV [57], E_A(6at%In) is fairly close to the linear combination of the activation energies of the pure elements (cf. $0.06 \cdot E_A(\text{In}) + 0.94 \cdot E_A(\text{Al}) = 270$ meV).

Measurements in liquid $Li_{64}Na_{36}$, which also has a miscibility gap, showed a deviation from the Arrhenius behavior close to the critical temperature [17].

Density measurements

Figure 8 shows the results of density measurements up to 20 at% In. The measured density values for pure Al agree very well with values in the literature [59, 60].

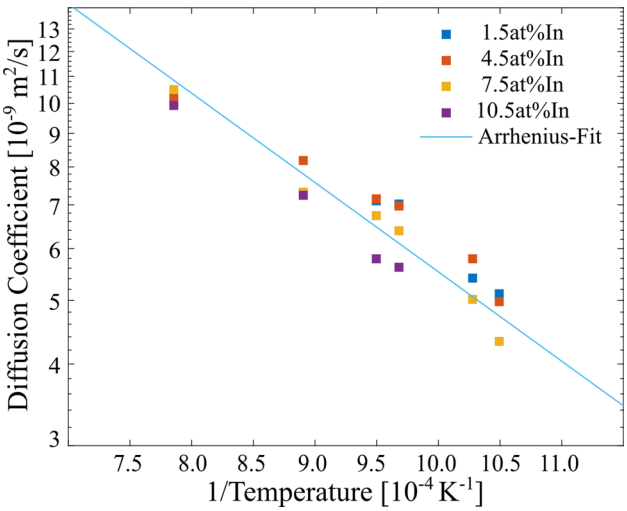

Figure 7 Diffusion coefficients as a function of inverse temperature in a semilogarithmic plot. The data were fitted with an Arrhenius function: $D_0 = (12.8 \pm 2.7) \cdot 10^{-8}$m^2/s and $E_A = 271 \pm 27$ meV. It represents the temperature dependence for the average composition (~ 6at%In) of all measurements.

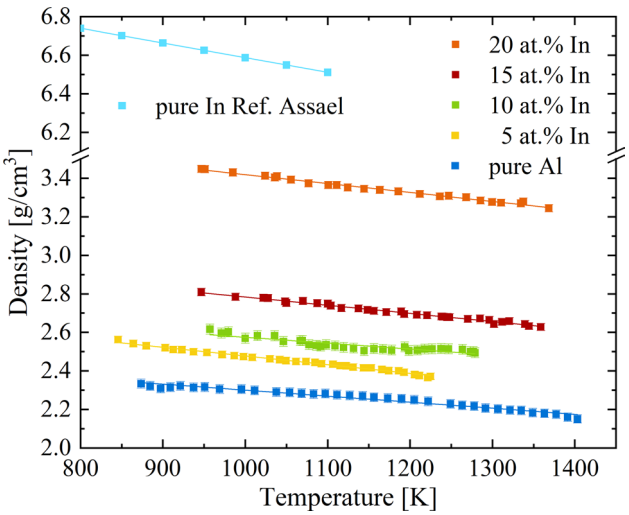

Figure 8 Results of density measurements using EML technique. Reference: Assael et al. [58]. The errorbars are roughly the size of the symbols.

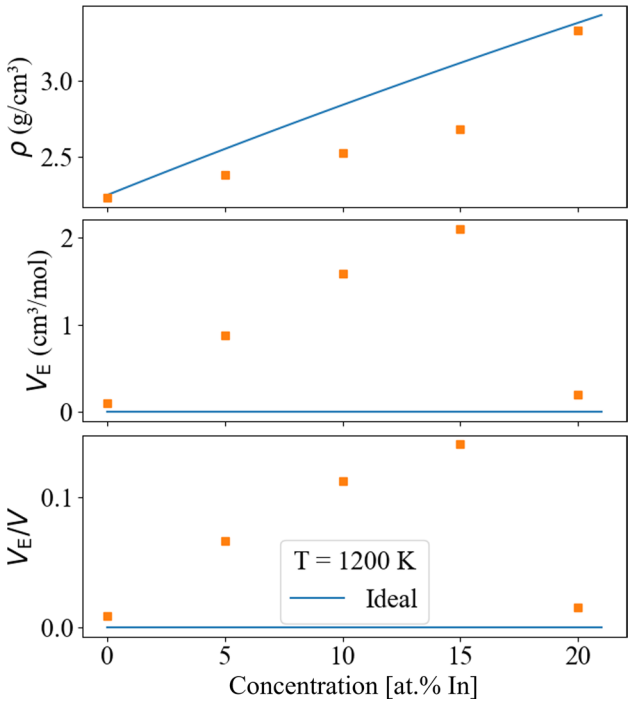

Figure 9 Determined densities, excess volume and relative excess volume at 1200 K as function of In concentration compared to the ideal behavior.

Table 1 Parameters T_L, ρ_L and ρ_T as in Eq. (6) for the density measurements in liquid Al–In

Composition	T_L [K]	ρ_L [g cm^{-3}]	ρ_T [g cm^{-3} K^{-1}]
Al	933.5	2.33	-3.80×10^{-4}
$Al_{95}In_5$	910.9	2.51	-4.32×10^{-4}
$Al_{90}In_{10}$	910.9	2.59	-2.22×10^{-4}
$Al_{85}In_{15}$	910.9	2.81	-4.43×10^{-4}
$Al_{80}In_{20}$	910.9	3.44	-4.00×10^{-4}

The temperature dependence of each composition can be described by a linear fit where the density $\rho(T)$ is given by the density at the liquidus temperature, ρ_L, the slope $\rho_T = \partial\rho/\partial T$ and the liquidus temperature T_L via

$$\rho(T) = \rho_L + \rho_T(T - T_L) \tag{6}$$

The parameters for each fit are compiled in Table 1.

It should be noted at this point that the density measurements were also carried out within the miscibility gap. This is possible as long as the sample can be further levitated, and its surface does not deform too much asymmetrically. Within the sphere, segregation will take place, but the melt will be constantly recirculated by induced convection.

For example at 950 K, the composition of 20 at% In is already well inside the miscibility gap. Nevertheless, this is not noticeable in the temperature dependence of density. Both above and below the segregation temperature, which is found for that composition at about 1100 K, the thermal expansion of the melt is the same.

If the density is plotted as a function of In concentration (see Fig. 9), it is clear that the density increases with increasing In concentration. However, densities between 5 and 15 at% In are found below the ideal solution. Molecular dynamic simulation of Lennard–Jones models shows that the excess volume can be negative and positive for both demixing and fully miscible systems and that its behavior is governed by an interplay between the repulsive and attractive interactions [13].

Density measurements in demixing liquid Li-Na [17] and Bi-Ga [15] showed only insignificant deviations from the ideal behavior with a relative value of the excess volume of less than 0.1%. Khairulin et al. [61] reported an insignificant relative excess volume of not more than 0.4% for liquid Al–In. However, our measurements show a relative excess volume of up to 14%.

The measured density can be used to calculate the effective volume packing fraction F of the melt, assuming that the atoms can be represented by hard spheres with their respective covalent radius. The volume packing fraction is calculated via

$$F = \left(\frac{4\pi}{3}\sum_i c_i r_i^3\right) \Big/ \left(\frac{M}{\rho N_A}\right) \tag{7}$$

with c_i the molar concentration and r_i the covalent radius of element i, M the molar mass of the alloy and ρ its density.

With the covalent radii 142 pm for indium and 121 pm for aluminum, volume packing fractions between 0.33 and 0.38 from the measured densities at 1200 K are calculated. This is considerably lower than for other liquid alloys, e.g., Ge_2Ni (0.43) or $Zr_{64}Ni_{36}$ (0.55) at the same temperature [62].

As mentioned before, low packing fraction is associated with fast self-diffusion [26, 27]. The result from density measurements therefore supports the idea that the contribution from self-diffusion counteracts the decrease of the thermodynamic factor leading to a weak concentration dependence of interdiffusion.

Conclusion

We used a shear cell furnace in combination with X-radiography to obtain in situ data on interdiffusion in liquid Al-rich Al–In alloys. Al–In, as a typical monotectic alloy, shows a demixing behavior for medium concentrations. The thermodynamic factor is derived from the Gibbs energy of a mixture and is equal to unity for ideal mixtures. It is below unity for mixtures with a miscibility gap and is zero where the spinodal decomposition starts. When approaching the miscibility gap, the thermodynamic factor decreases rapidly. According to Darken's equation, interdiffusion is given by a kinetic contribution, containing the self-diffusion coefficients, multiplied by the thermodynamic factor. Therefore, a steep decrease of the interdiffusion coefficient would be expected when approaching the miscibility gap. However, our data only show a slight decrease. This could be explained by an increase of the self-diffusion or by the factor S, which is also contained in the kinetic contribution to the interdiffusion coefficient. Future self-diffusion measurements in Al–In melts will clarify this open question. The temperature dependence of interdiffusion can be described by an Arrhenius fit with an activation energy of 270 meV, which is close to the activation energy of pure liquid aluminum.

Using electromagnetic levitation, we measured the density of Al-rich Al–In melts in temperature ranges where the alloy was fully mixed, as well as in the demixed phase. There is no visible change in the temperature dependence of the density when transitioning from the mixed to the demixed phase. The excess volume is negative, with more than 10% relative excess volume for 10 to 15 at% In. Although demixing alloys may show positive or negative excess volume, such a large deviation from the ideal behavior has not been reported in any other demixing liquid alloy.

The volume packing fraction can be calculated from the density. For Al-rich Al–In, the volume packing fraction is very low compared to other metallic melts. Low volume packing fractions usually mean fast self-diffusion. This is an additional hint that the kinetic contributions to interdiffusion are more important than the thermodynamic contributions to interdiffusion in liquid Al-rich Al–In.

Acknowledgements

We thank Jürgen Brillo for a critical reading of the manuscript.

Funding

Open Access funding enabled and organized by Projekt DEAL.

Declarations

Conflict of interest The authors have no relevant financial or non-financial interests to disclose.

References

[1] Kaban I, Köhler M, Ratke L, Nowak R, Sobczak N, Mattern N, Eckert J, Greer AL, Sohn SW, Kim DH (2012) Phase separation in monotectic alloys as a route for liquid state fabrication of composite materials. J Mater Sci 47(24):8360–8366. https://doi.org/10.1007/s10853-012-6660-3

[2] Zhou B, Lin W, Liu Y, Zheng T, Zhong Y, Wang H, Wang Q (2021) Effects of high static magnetic field on the microstructure of Zn–Bi monotectic alloys during directional solidification process. J Alloy Compd 889:161670. https://doi.org/10.1016/j.jallcom.2021.161670

[3] Freitas ES, Spinelli JE, Casteletti LC, Garcia A (2013) Microstructure-wear behavior correlation on a directionally solidified Al–In monotectic alloy. Tribol Int 66:182–186. https://doi.org/10.1016/j.triboint.2013.05.009

[4] Yasuda H, Ohnaka I, Fujimoto S, Sugiyama A, Hayashi Y, Yamamoto M, Tsuchiyama A, Nakano T, Uesugi K, Kishio K (2004) Fabrication of porous aluminum with deep pores by using Al–In monotectic solidification and electrochemical etching. Mater Lett 58(6):911–915. https://doi.org/10.1016/j.matlet.2003.07.032

[5] Ratke L, Müller A, Seifert M, Kapserovich G (2010) Monotectic alloys and their growth morphologies. Mater Sci Forum 649:137–142

[6] Hüter C, Boussinot G, Brener EA, Temkin DE (2011) Solidification along the interface between demixed liquids in monotectic systems. Phys Rev E 83(5):050601

[7] Laxmipathy VP, Wang F, Selzer M, Nestler B (2020) Microstructural transition in monotectic alloys: a phase-field study. Int J Heat Mass Transf 159:120096. https://doi.org/10.1016/j.ijheatmasstransfer.2020.120096

[8] Divilov S, Eckert H, Toher C, Friedrich R, Zettel AC, Brenner DW, Fahrenholtz WG, Wolfe DE, Zurek E, Maria J-P, Hotz N, Campilongo X, Curtarolo S (2024) A priori procedure to establish spinodal decomposition in alloys. Acta Mater 266:119667

[9] Zafari A, Xia K (2021) Nano/ultrafine grained immiscible Fe–Cu alloy with ultrahigh strength produced by selective laser melting. Mater Res Lett 9(6):247–254. https://doi.org/10.1080/21663831.2021.1884620

[10] Wang Y, Zhang L, Luo J, Qi L (2024) Evaluation of the segregation in printed mono-sized Al–In alloy droplets. J Mater Process Technol 326:118339. https://doi.org/10.1016/j.jmatprotec.2024.118339

[11] Kim SS, Sanders TH (2006) Thermodynamic assessment of the metastable liquidi in the Al–In, Al–Bi and Al–Pb systems. Modell Simul Mater Sci Eng 14(7):1181–1188. https://doi.org/10.1088/0965-0393/14/7/006

[12] Singh RN, Sommer F (1997) Segregation and immiscibility in liquid binary alloys. Rep Prog Phys 60(1):57–150. https://doi.org/10.1088/0034-4885/60/1/003

[13] Amore S, Horbach J, Egry I (2011) Is there a relation between excess volume and miscibility in binary liquid mixtures? J Chem Phys. https://doi.org/10.1063/1.3528217

[14] Abdellah AB, Gasser JG, Bouziane K, Grosdidier B, Busaidi M (2007) Experimental procedure to determine the interdiffusion coefficient of miscibility gap liquid alloys: case of GaPb system. Phys Rev B 76(17):174203

[15] Khairulin RA, Stankus SV, Sorokin AL (2002) Determination of the two-melt phase boundary and study of the binary diffusion in liquid Bi–Ga system with a miscibility gap. J Non-Cryst Solids 297:120–130

[16] Bräuer P, Müller-Vogt G (1998) Measurements of aluminum diffusion in molten gallium and indium. J Cryst Growth 186(4):520–527

[17] Khairulin RA, Abdullaev RN, Stankus SV (2019) Phase equilibria and mutual diffusion in liquid lithium-sodium alloys. J Eng Thermophys 28(4):472–483

[18] Inui M, Takeda S, Uechi T (1992) Ultrasonic velocity and density measurement of liquid Bi–Ga alloys with Miscibility Gap Region. J Phys Soc Jpn 61:3203–3208. https://doi.org/10.1143/jpsj.61.3203

[19] Yagodin DA, Filippov VV, Popel PS, Sidorov VE, Son LD (2008) Density and ultrasound velocity in ga–bi melts. J Phys: Conf Ser 98(6):062019. https://doi.org/10.1088/1742-6596/98/6/062019

[20] Cussler EL (2009) Diffusion: mass transfer in fluid systems. Cambridge University Press, Cambridge

[21] Reinhart G, Browne DJ, Kargl F, García-Moreno F, Becker M, Sondermann E, Binder K, Mullen JS, Zimmermann G, Mathiesen RH, Sillekens WH, Nguyen-Thi H (2023) In-situ x-ray monitoring of solidification and related processes of metal alloys. npj Microgravity. https://doi.org/10.1038/s41526-023-00321-z

[22] Schiller T, Sondermann E, Meyer A (2021) New analyzing approaches for in situ interdiffusion experiments to determine concentration-dependent diffusion coefficients in liquid Al–Au. Metals 11(11):1772

[23] Sondermann E, Jakse N, Binder K, Mielke A, Heuskin D, Kargl F, Meyer A (2019) Concentration dependence of interdiffusion in aluminum-rich Al–Cu melts. Phys Rev B 99(2):024204

[24] Griesche A, Zhang B, Solórzano E, Garcia-Moreno F (2010) Note: X-ray radiography for measuring chemical diffusion in metallic melts. Rev Sci Instrum 81(5):056104

[25] Okamoto H (2012) Al-In (aluminum-indium). J Phase Equilib Diffus 33(5):413–413

[26] Kuhn P, Horbach J, Kargl F, Meyer A, Voigtmann T (2014) Diffusion and interdiffusion in binary metallic melts. Phys Rev B 90(2):024309. https://doi.org/10.1103/PhysRevB.90.024309

[27] Li J, Zhao G, Chen Y, Wang J, Li X, Qin J (2025) Composition-dependent atomic transport properties of liquid Ti–Al alloys: Correlation between local structure and dynamic behavior. J Chem Phys. https://doi.org/10.1063/5.0288652

[28] Darken LS (1948) Diffusion, mobility and their interrelation through free energy in binary metallic systems. Trans Aime 175:184–201

[29] Horbach J, Das SK, Griesche A, Macht M-P, Frohberg G, Meyer A (2007) Self-diffusion and interdiffusion in Al

80 Ni 20 melts: simulation and experiment. Phys Rev B 75(17):174304
[30] Yang F, Heintzmann P, Kargl F, Binder K, Nowak B, Schillinger B, Voigtmann T, Meyer A (2018) Kinetics-dominated interdiffusion in metallic glass-forming liquids. Phys Rev B 98:064202. https://doi.org/10.1103/PhysRevB.98.064202
[31] Manning JR (1961) Diffusion in a chemical concentration gradient. Phys Rev 124(2):470
[32] Griesche A, Macht M, Frohberg G (2007) Diffusion in metallic melts. Def Diffus Forum 266:101–108
[33] Griesche A, Zhang B, Horbach J, Meyer A (2010) Interdiffusion and thermodynamic forces in binary liquid alloys. Mater Sci Forum 649:481–486. https://doi.org/10.4028/www.scientific.net/msf.649.481
[34] Neumann C, Sondermann E, Kargl F, Meyer A (2011) Compact high-temperature shear-cell furnace for in-situ diffusion measurements. J Phys: Conf Ser 327:012052
[35] Sondermann E, Neumann C, Kargl F, Meyer A (2013) Compact high-temperature shear-cell furnace for in-situ interdiffusion measurements. High Temp-High Press 42(1):23
[36] Meyer A (2010) Self-diffusion in liquid copper as seen by quasielastic neutron scattering. Phys Rev B 81(1):012102
[37] Meyer A, Hennig L, Kargl F, Unruh T (2019) Iron self diffusion in liquid pure iron and iron-carbon alloys. J Phys: Condens Matter 31(39):395401
[38] Sondermann E, Voigtmann T, Meyer A (2022) Influence of gravity on atomic mobility in a liquid. Micrograv Sci Technol 34(5):93
[39] Jalbert LB, Banish RM, Rosenberger F (1998) Real-time diffusivity measurements in liquids at several temperatures with one sample. Phys Rev E 57:1727–1736. https://doi.org/10.1103/PhysRevE.57.1727
[40] Kobayashi Y, Shiinoki M, Kato S, Masaki T, Suzuki S (2023) Elimination of systematic error in diffusion measurement using in-situ x-ray fluorescence analysis for liquid alloys. Int J Microgravity Sci Ap. https://doi.org/10.15011/jasma.40.400403
[41] Ahmed T, Belova IV, Evteev AV, Levchenko EV, Murch GE (2015) Comparison of the Sauer-Freise and Hall methods for obtaining interdiffusion coefficients in binary alloys. J Phase Equilib Diffus 36(4):366–374
[42] Olaye O, Ojo O (2021) A new analytical method for computing concentration-dependent interdiffusion coefficient in binary systems with pre-existing solute concentration gradient. J Phase Equilib Diffus 42(2):303–314
[43] Crank J (1975) The mathematics of diffusion. Clarendon Press, Oxford
[44] Engelhardt M, Meyer A, Yang F, Simeoni G, Kargl F (2016) Self and chemical diffusion in liquid Al–Ag. Def Diffus Forum 367:157–166
[45] Kargl F, Sondermann E, Weis H, Meyer A (2013) Impact of convective flow on long-capillary chemical diffusion studies of liquid binary alloys. High Temp-High Press 42(1):3
[46] Brillo J, Yang F, Holland-Moritz D (2024) Transport property measurement of liquid metals and alloys using electromagnetic and electrostatic levitation. Int J Thermophys. https://doi.org/10.1007/s10765-023-03309-9
[47] Brillo J, Lohöfer G, Hohagen FS, Schneider S, Egry I (2006) Thermophysical property measurements of liquid metals by electromagnetic levitation. Int J Mater Prod Technol 26(3/4):247–273. https://doi.org/10.1504/ijmpt.2006.009469
[48] Brillo J (2016) Thermophysical properties of multicomponent liquid alloys. Walter de Gruyter GmbH, Berlin
[49] Reiplinger B, Brillo J (2022) Density and excess volume of the liquid Ti–V system measured in electromagnetic levitation. J Mater Sci 57(16):7954–7964. https://doi.org/10.1007/s10853-022-07090-2
[50] Reiplinger B, Plevachuk Y, Brillo J (2023) Experimental study of density, molar volume and surface tension of the liquid Ti–V system measured in electromagnetic levitation. High Temp-High Press 52(2):175–190. https://doi.org/10.32908/hthp.v52.1355
[51] Kargl F, Weis H, Unruh T, Meyer A (2012) Self diffusion in liquid aluminium. J Phys: Conf Ser 340:012077
[52] Sondermann E, Kargl F, Meyer A (2016) Influence of cross correlations on interdiffusion in Al-rich Al–Ni melts. Phys Rev B 93(18):184201
[53] Foster J, Reynik R (1973) Self-diffusion in liquid tin and indium over extensive temperature ranges. Metallu Trans 4(1):207–216
[54] Kaban I, Curiotto S, Chatain D, Hoyer W (2010) Surfaces, interfaces and phase transitions in Al–In monotectic alloys. Acta Mater 58(9):3406–3414
[55] Qi Y, Wang L, Fang T (2013) Demixing behaviour in binary Cu–Co melt. Phys Chem Liq 51(6):687–694
[56] Das SK, Fisher ME, Sengers JV, Horbach J, Binder K (2006) Critical dynamics in a binary fluid: simulations and finite-size scaling. Phys Rev Lett 97(2):025702
[57] Nachtrieb N (1967) Structure of liquid metals. Adv Phys 16(62):309–323
[58] Assael MJ, Armyra IJ, Brillo J, Stankus SV, Wu J, Wakeham WA (2012) Reference data for the density and viscosity of liquid cadmium, cobalt, gallium, indium, mercury, silicon, thallium, and zinc. J Phys Chem Ref Data 41(3):033101. https://doi.org/10.1063/1.4729873

[59] Peng H, Voigtmann T, Kolland G, Kobatake H, Brillo J (2015) Structural and dynamical properties of liquid Al–Au alloys. Phys Rev B 92(18):184201

[60] Schmitz J, Hallstedt B, Brillo J, Egry I, Schick M (2012) Density and thermal expansion of liquid Al–Si alloys. J Mater Sci 47:3706–3712. https://doi.org/10.1007/s10853-011-6219-8

[61] Khairulin RA, Stankus SV (1996) Phase equilibrium in indium–aluminum melts. Russ J Phys Chem 70(7):1144–1146

[62] Nell S, Yang F, Evenson Z, Meyer A (2021) Viscous flow and self-diffusion in densely and loosely packed metallic melts. Phys Rev B 103(6):064206